Incorporation mechanism of colloidal TiO_2 nanoparticles and their effect on properties of coatings grown on 7075 Al alloy from silicate-based solution using plasma electrolytic oxidation

Mehri HASHEMZADEH[1], Keyvan RAEISSI[1], Fakhreddin ASHRAFIZADEH[1],
Amin HAKIMIZAD[2], Monica SANTAMARIA[3]

1. Department of Materials Engineering, Isfahan University of Technology, Isfahan 84156-83111, Iran;
2. Yekta Mobaddel Pars Co., Science and Technology Campus, Yazd University, Yazd 89158-18411, Iran;
3. Dipartimento di Ingegneria, Università di Palermo, Viale Delle Scienze, Ed. 6, 90128, Palermo, Italy

Abstract: Plasma electrolytic oxidation (PEO) was applied using a pulsed unipolar waveform to produce Al_2O_3−TiO_2 composite coatings from sol electrolytic solutions containing colloidal TiO_2 nanoparticles. The sol solutions were produced by dissolving 1, 3, and 5 g/L of potassium titanyl oxalate (PTO) in a silicate solution. Scanning electron microscopy, energy dispersive spectrometry, X-ray diffraction, and Raman spectroscopy were applied to characterizing the coatings. Corrosion behavior of the coatings was investigated using polarization and impedance techniques. The results indicated that TiO_2 enters the coating through all types of micro-discharging and is doped into the alumina phase. The higher level of TiO_2 incorporation results in the decrease of surface micro-pores, while the lower incorporation shows a reverse effect. It was revealed that the higher TiO_2 content makes a more compact outer layer and increases the inner layer thickness of the coating. Electrochemical measurements revealed that the coating obtained from the solution containing 3 g/L PTO exhibits higher corrosion performance than that obtained in the absence of PTO. The coating produced in the absence of PTO consists of γ-Al_2O_3, δ-Al_2O_3 and amorphous phases, while α-Al_2O_3 is promoted by the presence of PTO.

Key words: Al alloy; Al_2O_3−TiO_2 coating; plasma electrolytic oxidation; potassium titanyl oxalate; corrosion resistance

1 Introduction

Despite the high specific strength and toughness of 7075 Al alloy, its susceptibility to different kinds of localized corrosion such as pitting and intergranular corrosion is a major challenge in the aerospace industry. The most common surface treatment for aluminum alloys is hard anodizing, but 7075-T6 Al alloy does not accept hard anodizing appropriately due to its compositional heterogeneity arising from the intermetallic compounds [1]. Plasma electrolytic oxidation (PEO) is a surface treatment that drew attention in the last decades to prevail the deficiencies of the conventional and hard anodizing methods [2]. PEO process fulfills over the breakdown voltage of the oxide layer, which leads to electrical discharges that provide proper conditions for the production of the coatings containing oxides of metals present in the substrate as well as species incorporated from the electrolytic solution [3–5]. Being a multifactor-controlled physico-chemical process, the properties of PEO coatings depend on electrical parameters such as current density and waveform (i.e. frequency and duty cycle [6−10]), and on employed

electrolyte composition and temperature [8,10−12]. The porosity resulting from the micro-discharges, and the limited range of composition of the PEO coatings are two significant challenges [13]. An efficient way to tune microstructure and composition of the PEO coatings is the selection of the electrolyte.

Al_2O_3−TiO_2 composite coatings are very promising since they can retain the beneficial features of both TiO_2 and Al_2O_3 [14]. Indeed, adding titania to alumina improves its fracture toughness [15], wear resistance and corrosion resistance [16,17], and dielectric [18], and photocatalytic properties [19]. BAHRAMIAN et al [17] revealed that in-situ incorporating TiO_2 nanoparticles into the coating using DC power improves the corrosion resistance of the Al alloy by reducing the coating porosity. HAKIMIZAD et al [10] produced Al_2O_3−TiO_2 composite coatings from a silicate-based electrolyte (10 g/L liquid glass) by adding solid TiO_2 nanoparticles. When unipolar waveform was applied, the high level of micro-pores in the coating was responsible to fail the corrosion withstand. However, bipolar waveforms improved the corrosion performance of the coatings, which was attributed to the effective role of electrical parameters in increasing compactness and thickness of the coatings. A similar strategy was followed to produce Al_2O_3−TiO_2 composite coatings in the same silicate solution by adding potassium titanyl oxalate (PTO) as an ionic additive [20]. PTO created a sol electrolytic solution containing colloidal TiO_2 nanoparticles together with silicate. The coatings prepared in these conditions provided higher corrosion resistance than those grown using solid TiO_2 nanoparticles [10]. However, the PTO was considered as a fix constituent of the bath, and thus, its net effect on improving the coating microstructure was less studied.

In this study, to explore the precise effect of colloidal TiO_2 nanoparticles on microstructure and properties of Al_2O_3−TiO_2 composite coatings, PEO process was carried out at different PTO concentrations using a simple unipolar waveform to reduce the complexity of coating process. Regarding liquid glass and its complicated polymeric structure, we used sodium metasilicate pentahydrate as the silicate source in the electrolytic solution.

2 Experimental

2.1 Specimen preparation

Disc-shaped specimens of 7075 Al alloy with the chemical composition (wt.%) of 3.3 Mg, 5.8 Zn, 1.3 Cu, 0.3 Cr, 0.4 Fe, 0.2 Mn, and balance Al with the diameter of 20 mm and the width of 3 mm were used as substrates. Both faces of the specimens were mechanically polished down to 1200 grit using SiC abrasive papers. After connecting the specimens to copper wires, they were washed ultrasonically in deionized water and ethanol and finally dried in cold airflow.

2.2 Plasma electrolytic oxidation process

For the plasma electrolytic oxidation (PEO) treatment, a full-switching double isolated source power supply capable of delivering adjustable unipolar and bipolar waveforms up to 750 V/30 A was employed. A unipolar current at a constant frequency of 2 kHz, 20% duty cycle, and average anodic current density of 6 A/dm^2 was applied using the mentioned power supply. A 7 L cylindrical cell made of 316 L stainless steel was used, where its wall served as the counter electrode. The cell was placed in a 100 L water-filled temperature-controlled container. The inside electrolyte was vigorously stirred using a submersible full polymer-body electrical pump, maintaining the electrolyte temperature at (20±2) °C. The pretreated specimens and the container were connected to the positive terminal and the negative terminal of the power supply, respectively. The coating bath was prepared by dissolving 3 g/L sodium metasilicate pentahydrate ($Na_2SiO_3·5H_2O$, SMS) as the base electrolyte, 2 g/L KOH and potassium titanyl oxalate ($K_2TiO(C_2O_4)_2$, PTO) as an ionic additive in various concentrations. The specimen codes defined based on the PTO concentrations in the bath were P0, P1, P3, and P5, relating to 0, 1, 3, and 5 g/L PTO, respectively. The pH and conductivity values of the coating solutions are given in Table 1.

The coating process was performed for 60 min. For investigating the PTO role, the PEO treatment was performed in two electrolytes containing 0 and 3 g/L PTO for different time of 1, 1.5, 3, 5, 10, and 20 min.

Table 1 pH and conductivity of coating electrolytes containing different concentrations of PTO

Specimen code	pH	Conductivity/(mS·cm^{-1})
P0	12.32	9.3
P1	12.27	9.0
P3	12.13	8.2
P5	11.58	7.4

2.3 Coatings characterization

The surface and cross-section morphologies of the coatings were examined using a field emission scanning electron microscope (FESEM FEI Quanta feIg 450) equipped with an energy dispersive spectrometer (EDS) for determining the chemical composition and elemental maps of the coatings. After vertically mounting the specimens in an epoxy resin, the cross-sections were ground down to 2400 grit using abrasive SiC papers and polished to a mirror finishing using Buehler alumina powder (0.5 μm). Then, the specimens were cleaned ultrasonically in an ethanol bath, washed in deionized water, and dried in cold airflow. The average thickness of the coatings was estimated on cross-section of the SEM micrographs using Image J 1.44p software (version 1.6). The thickness values were measured in ten locations of each specimen, and the average value was reported.

The phase composition of the coatings was evaluated using a glancing-angle X-ray diffracto-meter (GAXRD, model ASENWARE A W-XDM300). The X-ray diffraction (XRD) patterns were obtained over a 2θ range of 20°−80° using Cu K$_\alpha$ radiation generated at 40 kV and 30 mA by the incident angle of 10°. X'pert Highscore software with PDF2 database was employed to analyze the XRD patterns.

Micro Raman spectrum was acquired using a Renishaw inVia Raman microscope spectrometer equipped with a microprobe and a CCD detector with a Nd:YAG laser of 532 nm.

2.4 Evaluation of corrosion behavior of coatings

Electrochemical impedance spectroscopy (EIS) tests were performed to investigate the corrosion behavior of the coatings, using a potentiostat/ galvanostat (AMETEK model PARSTAT 2273). The EIS tests were performed in 3.5 wt.% NaCl solution at pH 4, adjusted by adding dilute HCl solution, using a three-electrode cell. The pH was

decreased for intensifying the corrosive media and high-lightening the performance of the coating in the test [21]. A platinum plate and a saturated Ag/AgCl were applied as the counter and reference electrodes, respectively. The studied frequency range was from 10^{-2} to 10^5 Hz. The EIS tests were performed after 24 h immersion in the mentioned corrosive solution. Also, potentiodynamic polarization curves were recorded after 24 h immersion in the test solution. The potential range for these tests was from −250 mV versus open circuit potential (OCP) in the cathodic region to 500 mV versus OCP in the anodic region, at the scan rate of 1 mV/s. A minimum of three replicates were taken for each condition.

3 Results

3.1 Voltage−time response

Figure 1 shows the voltage−time curves obtained by applying a constant average current density of 6 A/dm^2 for 60 min in the presence of various PTO concentrations. Based on the slope variation of the curves, a typical four-stage voltage−time response is observed on each curve. The onsets of Stage III and IV are different at each PTO concentration and specified by the bullets in Fig. 1. The slopes of each stage are summarized in a table inserted in Fig. 1. The first stage (Stage I) is characterized by an abrupt linear increase of voltage versus time ascribed to the formation of a primary dielectric oxide film. After that, Stage II commences with the dielectric breakdown of the oxide film and the appearance of homogeneous fine
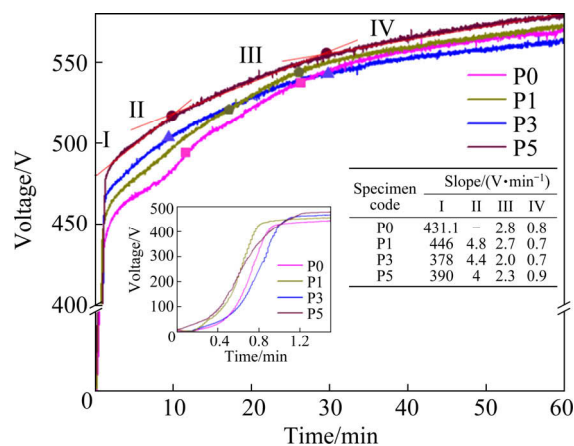

Fig. 1 Voltage−time graphs for specimens coated by PEO at different PTO concentrations (The inset table shows the slopes of four stages at different PTO concentrations)

white sparks. In Stage III, orange-red sparks occur, and the voltage continues to increase. This stage is known as the micro-arc stage. In Stage IV, the voltage variation is even lower than that of Stage III and reaches a near steady-state value similar to that in Refs. [22,23]. As observed in Fig. 1, the breakdown voltage is raised by increasing the PTO concentration. The breakdown voltage values in the electrolytes containing 0 and 5 g/L PTO are 419 and 467 V, respectively.

3.2 Microstructure and phase analysis

Figure 2 shows the surface morphologies of the PEO coatings. As observed, P0, P1, and P3 coatings exhibit a pancake morphology along with some fine particles attached to the pancakes, named

as the nodules in the literatures [2,24]. The density of nodules is reduced by increasing the PTO concentration. The size of the surface micro-pores is increased by adding 1 g/L PTO in the solution (Figs. 2(a, b)), while a reduction is seen at higher PTO concentrations (Figs. 2(c, d)). In electrolyte containing 5 g/L PTO (Fig. 2(d)), new protrusion structures named crater-like features appear on the coating surface. Also, micro-cracks are formed in the coatings due to thermal stress and high pressure [25]. The pancakes are created during discharging by the fast solidification of the melt thrown out from the coating/substrate interface. EDS analysis reveals that the pancakes are rich in Al element, (Fig. 3(a)), while the nodules are rich in Si and Ti elements (Fig. 3(b)).
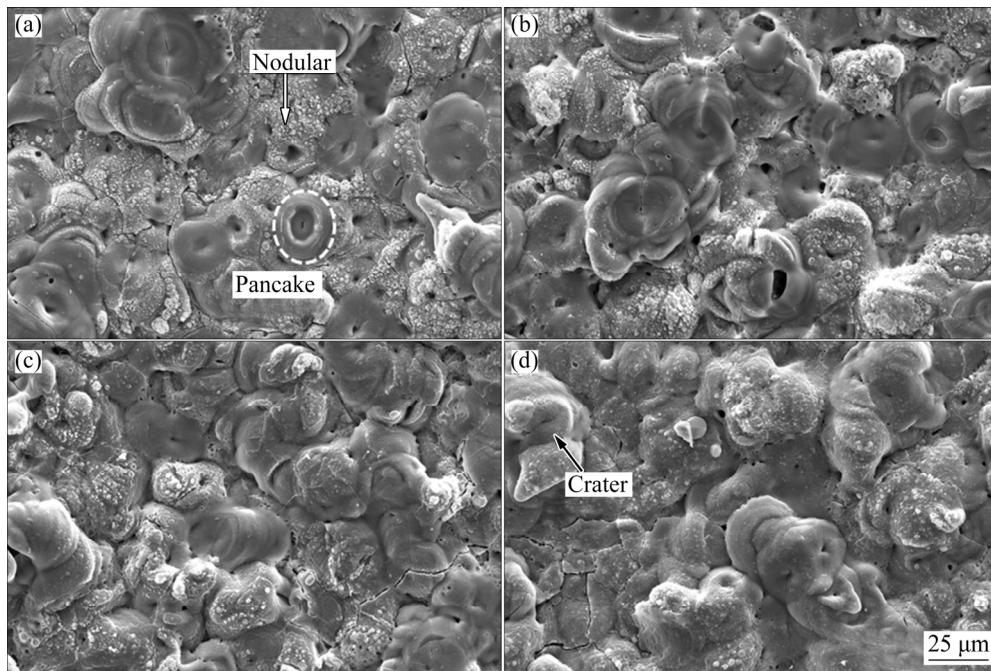

Fig. 2 Surface morphology images of PEO coatings prepared at different PTO concentrations: (a) P0; (b) P1; (c) P3; (d) P5
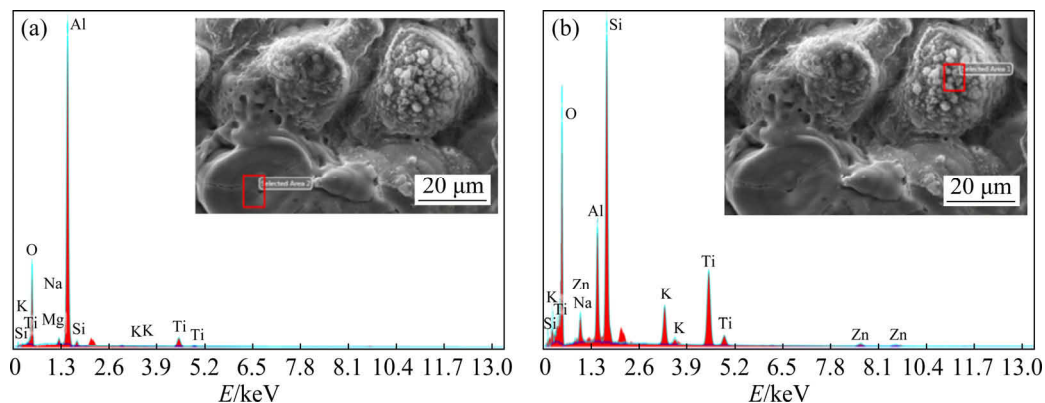

Fig. 3 EDS analysis on pancake (a), and nodular (b) structures

Table 2 gives surface elemental compositions of the PEO coatings obtained by EDS area analysis. The coating produced in PTO-free electrolyte (P0) mainly consists of Al, O, and Si. The increase of PTO concentration from 1 to 5 g/L raises the Ti incorporation in the coating from 1.3 to 7.8 at.%. However, the Si content is not influenced significantly. The presence of Si and Ti inside the coatings indicates that the electrolyte's species participate in the reactions occurring in the discharge channels and take part in the coating formation.

Figure 4 displays cross-sectional morphologies of the PEO coatings. A bi-layer coating is formed in all cases, with large lateral pores between the layers. In the absence of PTO (Fig. 4(a)), no clear inner layer can be detected in the coating, and many pores are present at the coating/substrate interface. However, adding 1 g/L PTO into the electrolyte creates a very thin inner layer, as seen in Fig. 4(b). By adding 3 and 5 g/L PTO in the electrolyte, the thickness of the inner layer and compactness of both inner and outer layers increase, although the coating thickness decreases from ~35 to ~29 μm (Figs. 4(c, d)). Therefore, it is reasonable to claim that the PTO is a modifier agent due to its capability for boosting the inner layer quality.

Figure 5 shows EDS elemental maps of Al, Mg, O, Si, and Ti of the coatings. As seen, Al, O, and Mg elements are distributed uniformly throughout the coatings. In the coating prepared from 0 and 1 g/L PTO (P0 and P1 specimens), Si is dominantly found on the coating surface, the inner walls of the pores, and at the coating/substrate interface. However, for the coatings grown in the presence of 3 and 5 g/L PTO (P3 and P5 specimens), Si is mostly accumulated in the upper layers of the coatings. In the P1 coating, Ti shows an even distribution, while in the P3 and P5 coatings, despite the presence of Ti throughout the coating, a dominant distribution is observed in the inner layer and even on the top surface of the coating.
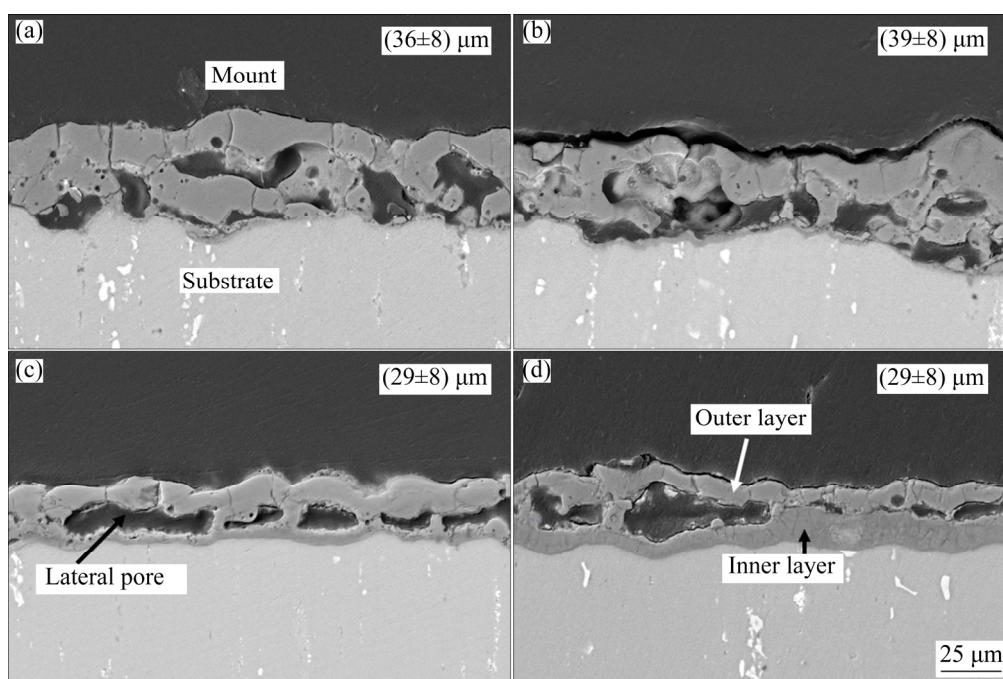
Table 2 Elemental composition from EDS analysis of prepared coatings (at.%)

Element	P0	P1	P3	P5
O	42.6	47.2	52.6	41.1
Na	2.9	2.2	2.0	2.3
Mg	1.1	1.2	0.6	0.7
Al	34.9	35.6	28.1	35.2
Si	16.4	10.7	8.3	10.8
K	2.0	1.8	1.9	2.0
Ti	−	1.3	6.4	7.8

Fig. 4 Cross-sectional SEM images of PEO coatings prepared at different PTO concentrations: (a) P0; (b) P1; (c) P3; (d) P5
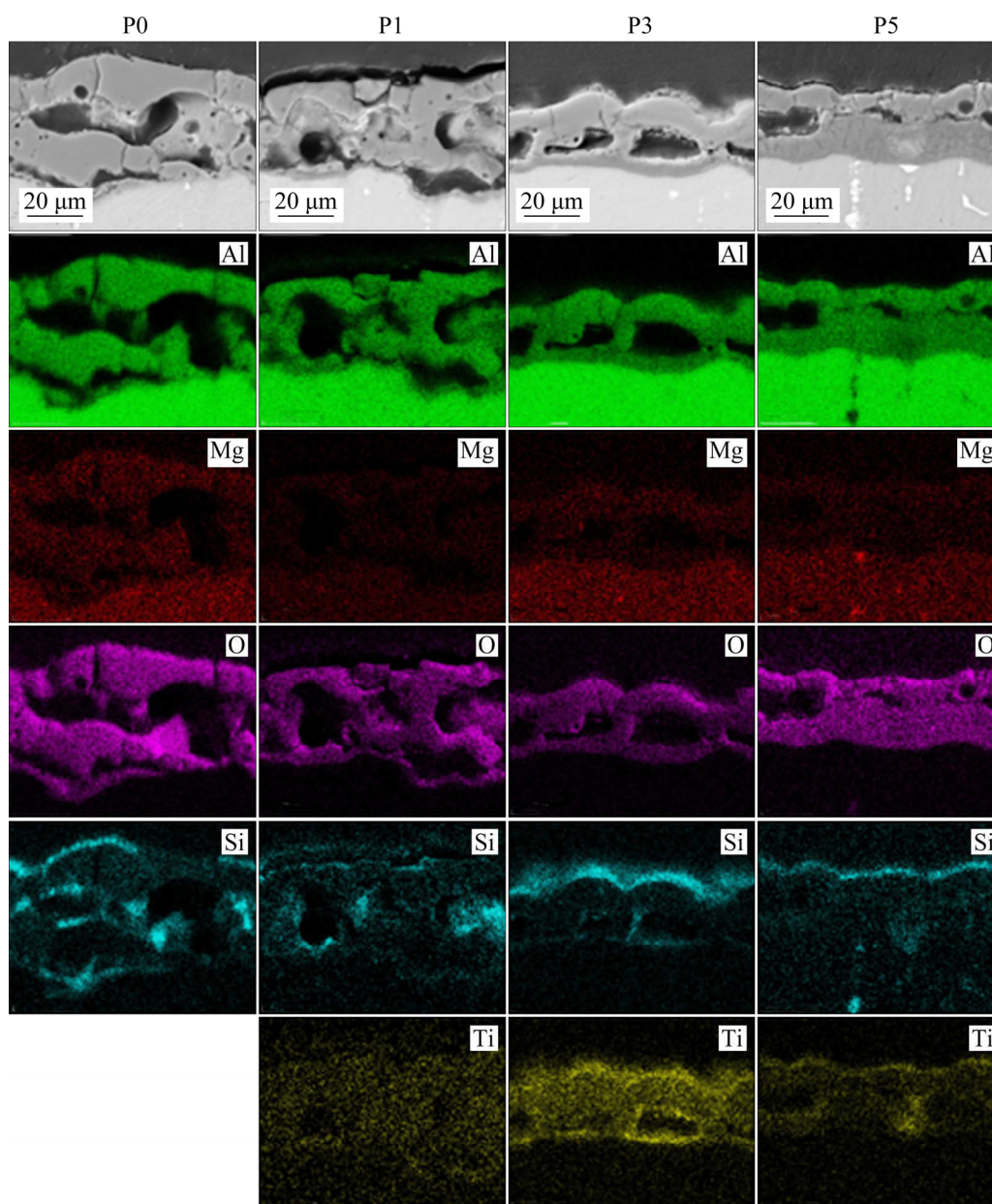
Fig. 5 Elemental mappings of PEO coatings produced in different electrolytes

Figure 6 displays XRD patterns of the coatings. In all specimens, the peaks related to Al alloy substrate, γ-Al_2O_3, and δ-Al_2O_3 are detected. By adding and increasing the PTO amount in the electrolyte, diffraction peaks of Al, γ-Al_2O_3, and δ-Al_2O_3 become weak, while the peaks related to α-Al_2O_3 become appear and intensify. The halo observed in the XRD patterns can be attributed to the significant presence of amorphous phases [26].

Figure 7 presents the Raman spectra of the P0, P3 and P5 specimens. In the Raman spectra, the broad peaks with relatively low intensities indicate that these phases have poor crystallinity. The Raman bands at 266 and 693 cm^{-1} are related to the
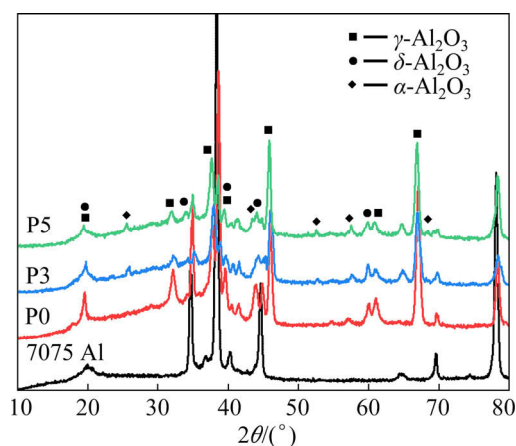

Fig. 6 XRD patterns of specimens coated by PEO in different electrolytes
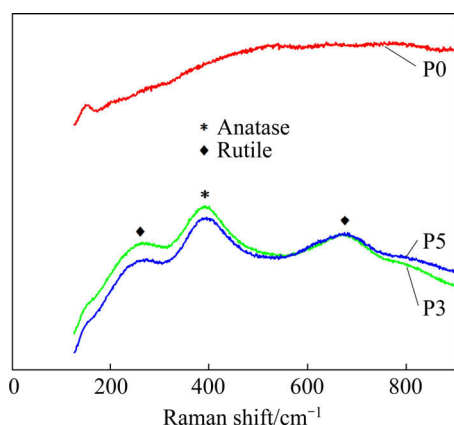
Fig. 7 Raman spectroscopy results of PEO coatings prepared from different electrolytes

doped rutile [27], and the band at 398 cm^{-1} matches to 2B1$_g$ active mode of anatase polymorph [28]. Indeed, the tetragonal structure of anatase belongs to the space group $D4h$ and has two formula units per primitive cell, leading to six Raman active phonons: 3E$_g$ (144, 196 and 638 cm^{-1}), 2B1$_g$ (398 and 519 cm^{-1}) and 1A1$_g$ (513 cm^{-1}) [28].

3.3 Corrosion behavior of coatings

Figure 8 displays potentiodynamic polarization curves employed to evaluate the corrosion behavior of the coated specimens in 3.5 wt.% NaCl solution (adjusted at pH 4 using hydrochloric acid).
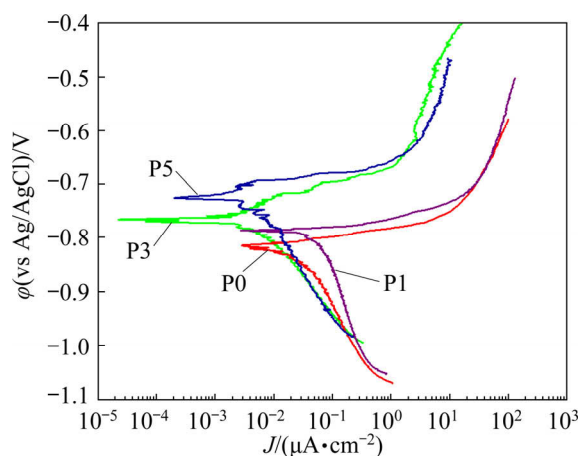

Fig. 8 Polarization curves of prepared coatings after 24 h immersion in 3.5 wt.% NaCl solution at pH 4

The electrochemical parameters including corrosion current density (J_{corr}), corrosion potential (φ_{corr}), and pitting potential (φ_{pit}) extracted from potentiodynamic polarization are given in Table 3.

For the P0 and P1 specimens, the anodic branch of the curve shows the onset of pitting

Table 3 values of electrochemical parameters extracted from potentiodynamic polarization plots recorded after 24 h immersion in 3.5 wt.% NaCl solution at pH 4

Specimen code	J_{corr}/ (nA·cm^{-2})	φ_{corr}(vs Ag/AgCl)/ mV	φ_{pit}(vs Ag/AgCl)/ mV
P0	25±7	−814±6	≈φ_{ocp}
P1	80±28	−795±7	≈φ_{ocp}
P3	5	−770±7	−719±6
P5	6±2.8	−733±10	−696±8

phenomena at potential very close to the corrosion potential (φ_{corr}). This means that the localized corrosion is possible at open circuit potential (OCP), i.e. the corrosion resistance of these coatings is very low. Better performances are shown by P3 and P5, whose breakdown potential is higher. EIS spectra were recorded to get more insight of the corrosion resistance of the coating and to highlight the role of the inner compact layer in influencing the corrosion resistance of the coatings. Nyquist and Bode-phase plots relating to the as-prepared coatings are shown in Fig. 9.

As seen in Bode-phase plots (Fig. 9(b)), all coatings reveal two humps. Both P0 and P1 specimens exhibit one hump at high-frequency region and another around 10 Hz. The high-frequency response is from the outer layer of the coating, while the low-frequency response is raised by the electrical double layer and the corresponding charge transfer [29]. This is because the paths created by pores/cracks in the outer layer of the coating locally expose the substrate surface to the corrosive solution, which results in the localized corrosion attack of the substrate [30]. This is in agreement with the polarization curves showing the local attack at OCP condition for P0 and P1 specimens (Fig. 8).

The electrical equivalent circuit (EC) for simulating the spectra is specified by applying Z-view. The EC is based on χ^2 values ($\leq 10^{-3}$) and logical values obtained from the simulated data. χ^2 value as a measure of goodness of fitting is defined as

$$\chi^2 = \sum_{i=1}^{n} \left[\frac{(z_i'(\omega_{i,p^{\rightarrow}})-a_i)^2}{a_i^2 + b_i^2} + \frac{(z_i''(\omega_{i,p^{\rightarrow}})-b_i)^2}{a_i^2 + b_i^2} \right] \quad (1)$$

where z_i' and z_i'' are calculated values, ω_i, α_i, and b_i are empirical data values, and $p^{\rightarrow}$ parameter is connected to the model [31].

In the EC (Fig. 10), R_s is the uncompensated solution resistance, R_{out} is the outer layer resistance of the coating, and R_{ct} is interfacial charge transfer resistance.

CPE is the constant phase element, which is applied in the EC instead of capacitance because
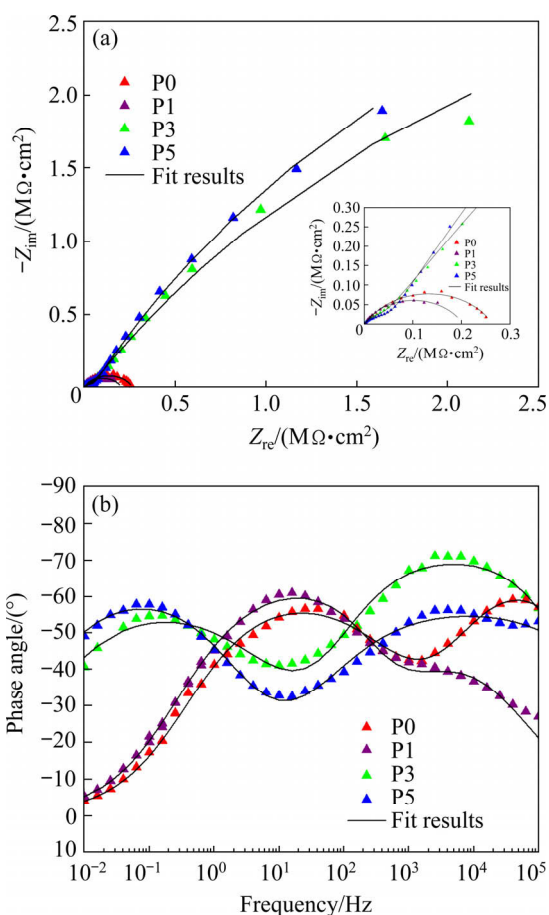

Fig. 9 Nyquist plots (a) and Bode-phase plots (b) of PEO coatings after 24 h immersion in 3.5 wt.% NaCl solution at pH 4
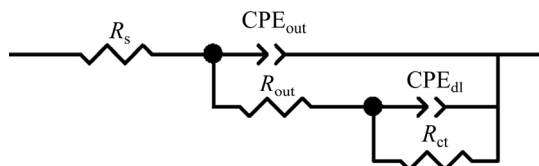

Fig. 10 Equivalent circuit of P0 and P1 specimens

often, the capacitance is not ideal. Porosity, roughness, cracks, and other intrinsic defects are some reasons for the non-ideal behavior of the PEO coatings [12]. The impedance representation of a CPE is calculated by

$$Z_{(CPE)}=1/[Q(j\omega)^n] \tag{2}$$

where Q and ω are the admittance and the angular frequency, respectively. Here $-1<n<1$ and the case $n=1$ belongs to an ideal capacitor [32]. CPE_{dl} and CPE_{out} refer to the constant phase elements of the electrical double layer and the outer layer of the coating.

For P3 and P5 specimens, the capacitive loops are de-convoluted well, as seen in Fig. 9(b). The loops at high frequencies are again attributed to the outer layers of the coatings, while the low-frequency ones are relating to the inner layers of the coating [33]. The corresponding EC is presented in Fig. 11, where R_{in} and CPE_{in} are responded by the inner layer resistance and inner layer capacitance of the coatings, respectively.

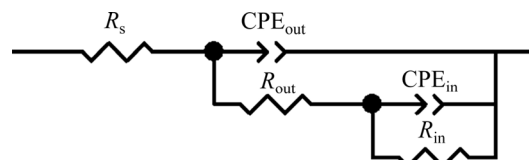The values of the electrical elements extracted by fitting the spectra are summarized in Table 4.

Fig. 11 Equivalent circuit of P3 and P5 specimens

3.4 Growth steps in PEO process

To reveal the precise role of PTO in PEO process, the coatings grown at different time from the baths containing 0 (P0) and 3 g/L PTO (P3) are traced. Figures 12 and 13 present surface and cross-sectional images of the P0 and P3 coatings, respectively, after various growing time.

As seen in Figs. 12(a) and 13(a), after 1 min processing, the coatings' surface is relatively flat, and a uniform nano-pore distribution is observed at

Table 4 Parameters extracted from Nyquist and Bode-phase plots in Fig. 9

Specimen code	$R_{out}/(k\Omega \cdot cm^2)$	$CPE_{out}/(\mu F \cdot s^{-1} \cdot cm^{-2})$	n_{out}	$R_{ct/in}/(M\Omega \cdot cm^2)$	$CPE_{dl/in}/(\mu F \cdot s^{-1} \cdot cm^{-2})$	$n_{dl/in}$
P0	1.8	0.2	0.8	0.3	1.9	0.7
P1	2.0	2.7	0.6	0.2	0.9	0.8
P3	49.2	0.2	0.8	10.0	1.5	0.6
P5	69.4	0.5	0.6	10.8	1.9	0.7

Fig. 12 Surface morphologies and cross-sectional SEM images of coatings prepared at different PEO time in electrolyte without PTO: (a, a′) 1 min; (b, b′) 1.5 min; (c, c′) 3 min; (d, d′) 5 min; (e, e′) 10 min; (f, f′) 20 min
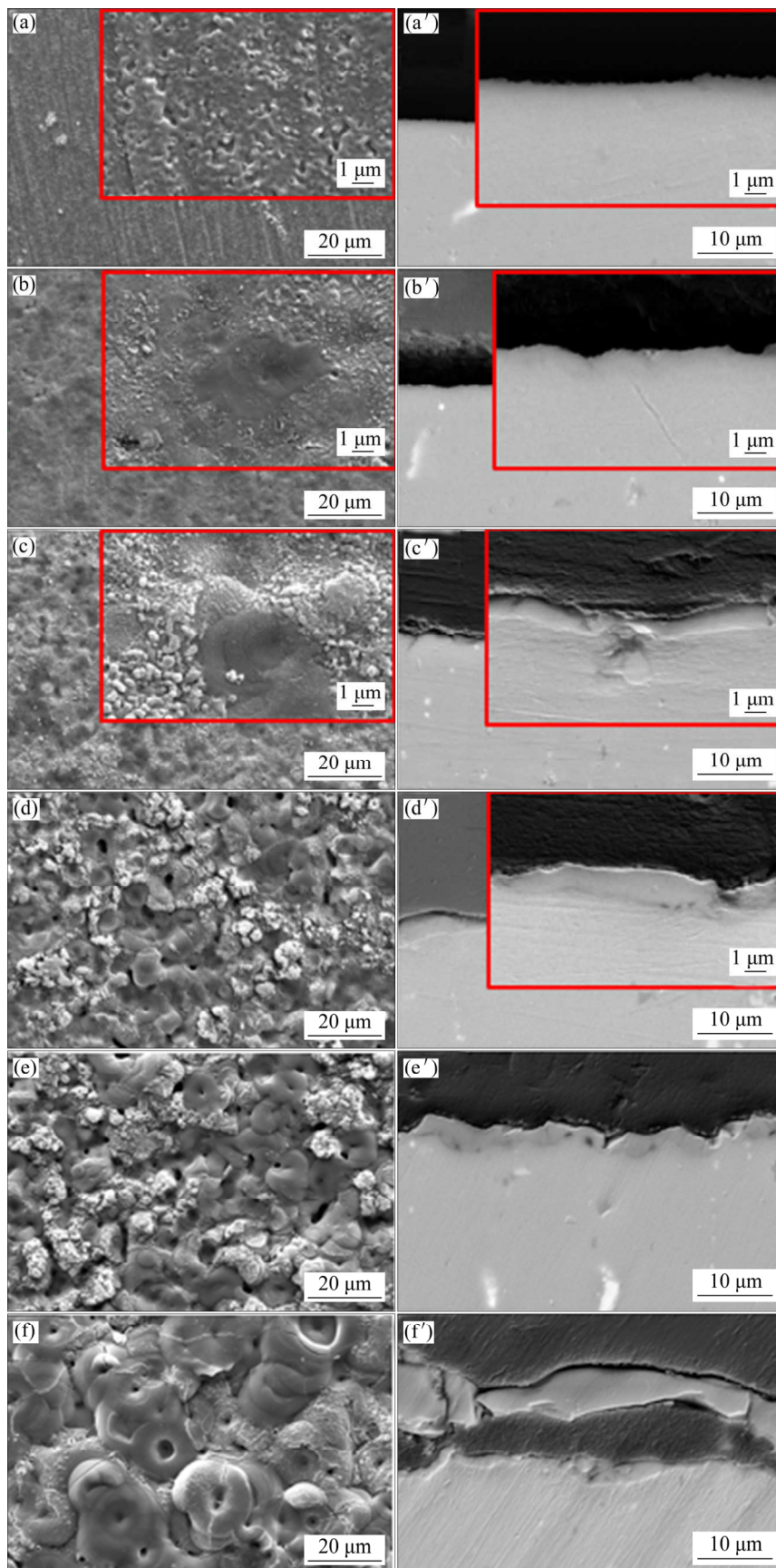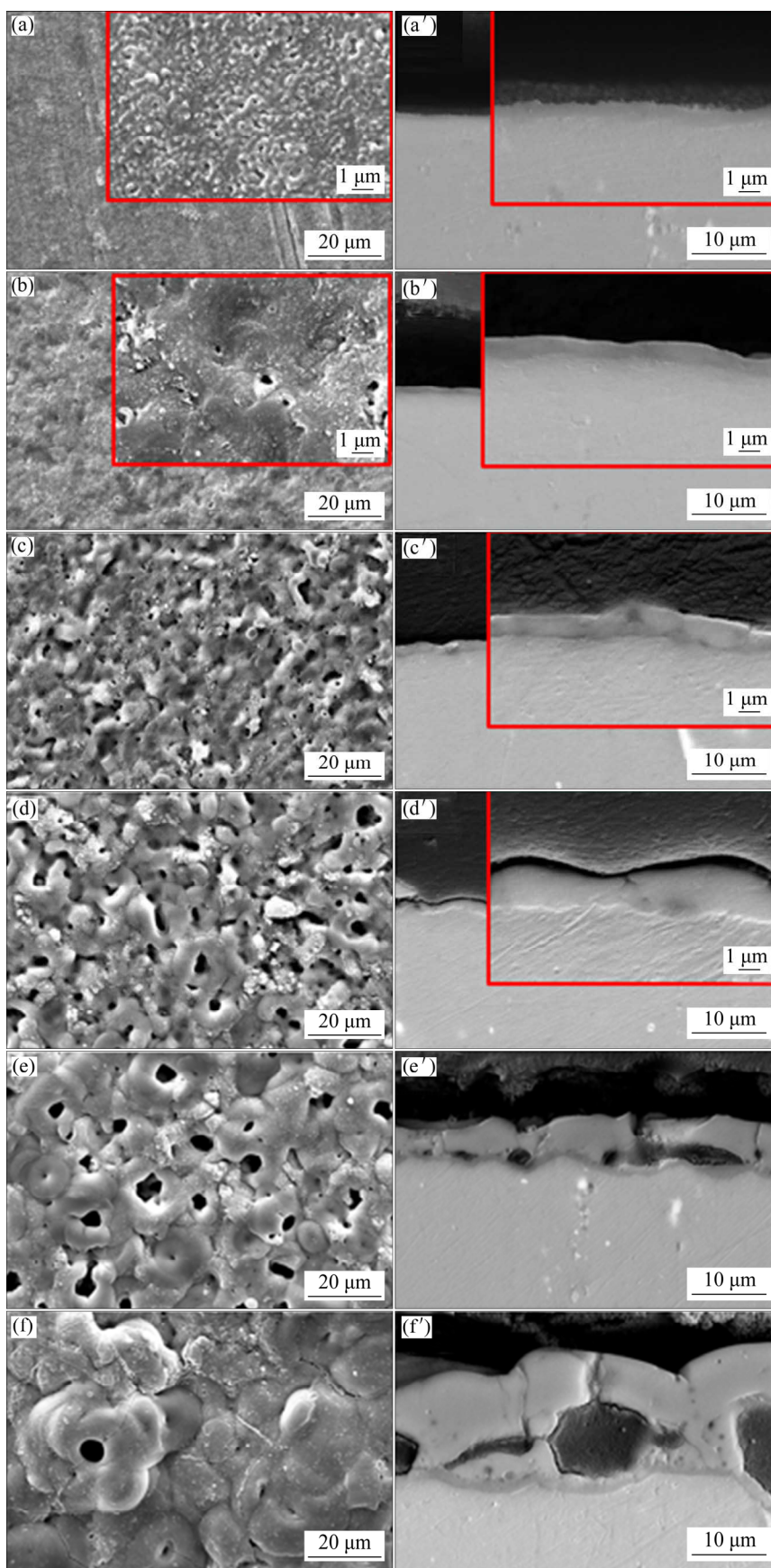
Fig. 13 Surface morphologies and cross-sectional SEM images of coatings prepared at different PEO time in electrolyte containing 3 g/L PTO: (a, a′) 1 min; (b, b′) 1.5 min; (c, c′) 3 min; (d, d′) 5 min; (e, e′) 10 min; (f, f′) 20 min

higher resolution. According to the corresponding cross-sections, a thin continuous barrier film is grown entirely on the substrate for P3 specimen (Fig. 13(a′)). However, the coating grown in the absence of PTO (P0) is very thin and some areas are observed bare (Fig. 12(a′)).

After the dielectric breakdown (1.5 min), the surface morphology of P3 coatings (Fig. 13(b)) consists of two regions, including a relatively smooth region rich in Al (dark) and a rough region rich in Ti and Si (white). The fine pores are also created due to the fine sparking occurring after dielectric breakdown [23]. The P3 specimen displays more discharge channels and its cross-section (Fig. 13(b′)) is thicker and denser than that of the P0 (Fig. 12(b′)). However, the surface morphology of the P0 coating undergoes a similar change as P3 coating after 3 min (Fig. 12(c)). At this time, the characteristic morphology of PEO coating appears for the P3 coating, where the pancakes with central holes are seen in Fig. 13(c). After 5 min, the pancakes also appear for the P0 coating (Fig. 12(d)). The cross-section of the P0 reveals a non-continuous porous layer (Fig. 12(d′)), while that of P3 seems sufficiently compact with a thickness of 1.3−2 μm (Fig. 13(d′)). By further increasing the time (Figs. 12(e, f) and Figs. 13(e, f)), the number of surface pores is reduced, and the pancakes become bigger. The comparison of Figs. 12(c, d, e) with Figs. 13(c, d, e) displays the larger micro-pores on the surface of P3 specimen. However, after 60 min coating growth (Fig. 2(c)), the micro-pores become significantly smaller.

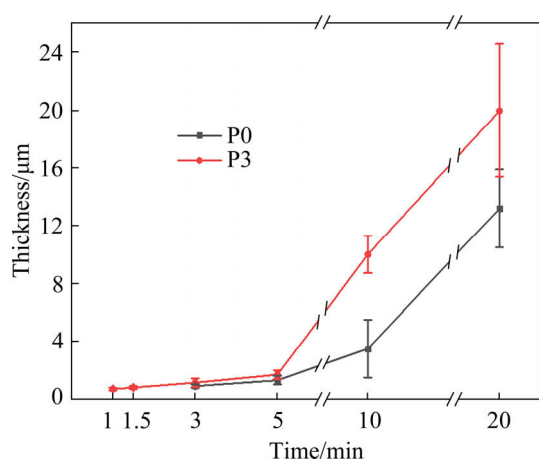The dependency of coating thickness on processing time is displayed in Fig. 14. A sudden

increment of thickness occurs after 5 min for both coatings. For P3 coating, the thickness versus time varies almost linearly from 5 to 20 min, with a growth rate of 0.9 μm/min.

Figure 15 shows the content variation of Si and Ti elements of P0 and P3 coatings with process time. The results show a decrease of Si content in both coatings at the initial stage of treatment. This is attributed to the excessive evolution of oxygen through plasma discharging. Contrary to the decline of Si content, the content of Ti increases right after the dielectric breakdown (1.5 min) for the P3 coating.
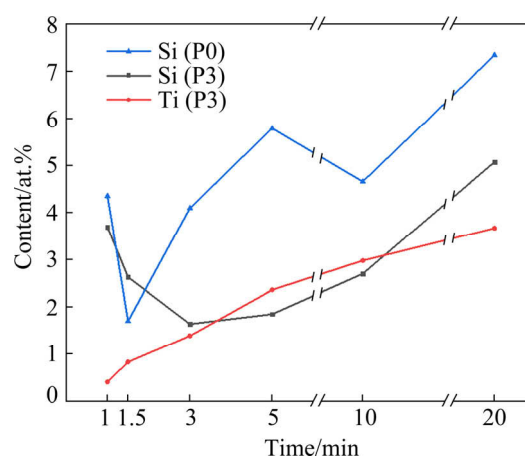
Fig. 15 Variation of Si and Ti element contents of coating with processing time in electrolyte containing 0 (P0) and 3 g/L PTO (P3)

4 Discussion

An approach to overcome intrinsic porosity and limited range of composition in PEO is to introduce appropriate additives into the coating bath aiming at their in-situ incorporation into the PEO coatings [13]. PTO salt, as an additive, dissolves in water to produce $TiO(C_2O_4)_2^{2-}$ and K^+ ions, as described in Eq. (3). In an alkaline solution, TiO_2 colloidal particles are also formed (Eq. (4)) [34]:

$$K_2[TiO(C_2O_4)_2] \rightarrow 2K^+ + [TiO(C_2O_4)_2^{2-}] \qquad (3)$$

$$[TiO(C_2O_4)_2^{2-}] + 2OH^- \rightarrow TiO_2 + H_2O + 2C_2O_4^{2-} \qquad (4)$$
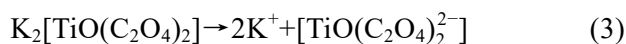
TiO_2 nano-particles are negatively charged [35] and, thus, they are driven toward the anode electrode by electrophoretic force in addition to mechanical admixture [36]. The colloidal TiO_2 nanoparticles generated inside the solution are significantly fine and easily incorporate into the coating. This is confirmed by the higher TiO_2

Fig. 14 Thickness of coatings prepared in electrolyte containing 0 and 3 g/L PTO at different PEO time

content of P3 coating in current study (~6.3 at.%) than that produced previously from the solution containing 3 g/L TiO_2 nanoparticles (~2.5 at.%) [10]. In Stage I of growing, the participation of decomposed products of PTO into the bottom pore of the created anodic films suppresses the dissolution of aluminum substrate [37]. Because TiO_2 is dominantly distributed in both inner layer and top surface of the coatings, it can be concluded that the various types of micro-discharging should be responsible for incorporating colloidal TiO_2 nanoparticles. On the other hand, since a gel of Si compounds is formed at the coating/solution interface [38], Si is abundant on top of the coating. The presence of Si in the inner layer of P0 and P1 coatings indicates that for these coatings, the solution reaches the inner layer via cracks, pores, or discharge channels during the PEO process [2].

Generally speaking, the PEO process involves two growth mechanisms. The first is the development of an outer layer far away from the substrate surface by micro-discharges releasing molten aluminum, which then solidifies and oxidizes immediately. The second is the development of an inner layer on the substrate surface that occurs through the inward oxygen diffusion [39]. According to HUSSEIN et al [40], the growth rate of the inner layer increases during the long treatment because of the thermal-activated diffusion nature of the PEO. It is reported that TiO_2, as a low-temperature sintering additive [41−43], decreases the sintering temperature of Al_2O_3, improves the distribution of melted alumina produced by micro-discharging, and thereby decreases the porosity of the resulted coating. Therefore, the outer layers of the coatings grown in the solutions containing 3 and 5 g/L PTO (Figs. 4(c, d)) are more compact than those produced in the absence and presence of lower PTO concentrations (Figs. 4(a, b)). For P0 and P1 coatings, the thickness is determined dominantly by the outer layer growth, while for P3 and P5 ones, it is determined by the inner layer growth. The lower growth rate of the outer layer in P3 and P5 finally results the less thickness values than P0 and P1, because the more compact outer layer limits the intensity and abundance of micro-discharges, which causes the lower releasement of molten

aluminum and then lower outer layer growth. Also, the TiO_2 weakens the binding forces in the alumina structure and enhances the oxygen diffusion in the matrix [44], and thereby, it increases the inner layer growth rate. It should be remarked that for the K_2TiF_6, a reverse effect was reported [45]. The fluoride ions released by ionization of this salt promote the field-assisted ejection of Al^{3+} ions from the surface of the oxide film, thereby reducing the efficiency of film growth [46].

There is a controversy about the formation mechanism of micro-pores at the inner/outer layer interface. As the processing time reaches 10 min, a single-layer with the thickness of (3.5 ± 2) μm is seen for the P0 coating (Fig. 12(e′)), while a fully-developed bi-layer structure appears in P3 coating (Fig. 13(e′)). The bi-layer structure is composed of a dark-contrast layer in direct touch with the substrate surface and an outer layer on top, associated with some pores between the two layers. However, the similar structure appears in P0 coating after 20 min (Fig. 12(f′)). To explain the formation of the pores between the inner and outer layers, three reasons are proposed: the dissolution of the coating and substrate by the electrolyte penetrated through open pores in the early stages [22], the flow of molten Al_2O_3 from the pore bottom toward the pore wall due to the growing stress and the field-assisted plasticity [47], and the excessive gas evolution under plasma discharging [2,48]. In the PEO process, the excessive oxygen evolution occurs due to the formation of OH^- radicals by ion bombardment of electrolyte species at the discharge/electrolyte interface [49]. The stress due to gas evolution drives the outer layer outward, and then, the pores will be formed at the interface of inner/outer layers. By considering the coating morphologies in Figs. 12 and 13 and the voltage−time responses in Fig. 1, it is deduced that the bi-layer structure is not created before the initiation of Stage III. In the mechanism proposed by CHENG et al [2,48], it is supposed that the lateral pores are formed soon after the dielectric breakdown. However, by considering Figs. 12(e′) and 13(d′), it is found that the lateral pores are not formed even after a significant dielectric breakdown.

In each processing time (except 60 min), the

thickness of the P3 coating is higher than that of the P0 coating due to the higher processing voltage governed (Fig. 1), which makes more strong arcs and results in higher molten material to emit supporting a thicker ceramic layer to be formed. Also, the dimension and number of discharge channels for P3 coating are higher than those of P0 coating at each time due to the higher driving force for tunneling ionization [50], supported by the lower conductivity of the electrolyte containing PTO (Table 1). A sudden increment of thickness that occurs after 5 min in both P0 and P3 coatings is due to the decrement of anodic dissolution. During anodizing, the current (I) flows across the oxide film in PEO process is the sum of the different processes including oxide coating formation, dissolution and oxygen evolution on the specimen surface:

$$I=I_i+I_e+I_d \tag{5}$$

where I_i, I_e, and I_d are the ionic current of the film growth, the electron current generated by oxygen evolution and the anodic dissolution current, respectively. In Stage I, when general anodizing process occurs, the total current is equal to the ionic one, while in Stage II, the rate of coating growth diminishes remarkably due to the anodic dissolution [51]. Anodic dissolution occurs intensively in thin films and withdraws suddenly by reaching the film thickness of 1−2 μm [52]. Then, after the formation of a thin film during the first 5 min, a sudden increment in the coating growth rate is seen.

At longer time, more intensive sparks, providing higher temperatures, melt the surface to fill the primarily created pores [53], and then the pore size decreases. Furthermore, refining the distribution of melted alumina by TiO$_2$ has a significant effect on decreasing the micro-pores in the P3 coating at longer processing time.

In PEO process, numerous micro discharges occur, which play important roles in the coating growth. Discharge events occurring in PEO process are named B-type discharges which originate from the substrate/coating interface, A-type and C-type discharges which occur in surface holes and relatively deep holes, respectively, and also D-type discharge occurring near the lateral pores [2,40].

The increase of Ti content at the early moments of Stage II (from 1 to 5 min) and Si content at longer time (from 5 to 20 min) (Fig. 15), indicates that the B-type discharges occurring at Stage II play the significant role in the incorporation of TiO$_2$ colloidal particles into the coating, while the Si incorporation occurs dominantly through A-type and C-type discharging at Stage III. At Stage III, the A-type and C-type discharges become dominant and the number of B-type discharges reduces significantly [40]. The nodular structures, rich in Si and Ti, approve the intensive incorporation of Si and Ti compounds into the coating through A-type and C-type discharges. The entrance of TiO$_2$ into inner layer should be attributed to the occurrence of D-type discharges.

By considering the effect of Ti content on the properties of the coating layers, the effect of PTO on voltage−time curve can be logically interpreted. At Stage II, the curve slope relating to P3 coating is higher than that of P0, where a denser and thicker coating is created. However, the slope inverses at Stage III. Here, the effective parameter seems to be the coating composition, where the higher Ti content entering the coating at the longer time raises the electrical conductivity of the P3 specimen and thus reduces the voltage required to keep the current density constant, as compared to that of P0 specimen [20]. Therefore, in Stage IV, the cell voltage of the coating process relating to P3 specimen is lower than that of P0. This reduces the destructive micro-discharges and thus decreases the thickness and porosity of the P3 coating. The increment observed in breakdown voltage with adding PTO is in agreement with the decrease in electrolyte conductivity (Table 1).

The PEO creates various major and minor phases in the coating. The γ-Al$_2$O$_3$ and δ-Al$_2$O$_3$ are metastable polymorphs of alumina, while α-Al$_2$O$_3$ (corundum) is a thermodynamically stable polymorph. The lack of Si compound peaks in the XRD patterns indicates that this element should be incorporated as an amorphous phase. This is because the interfacial temperature during the PEO process is lower than 1723 °C, not enough for the crystallization of silica [26]. The shift of alumina characteristic peaks, especially γ-Al$_2$O$_3$, to the lower angles along with the peaks broadening confirms

that the alumina phases are doped by TiO_2, which is in agreement with the Raman spectra (Fig. 7). In the PEO treatment, the high rate of heat dissipation to both substrate and electrolyte leads to a high cooling rate of the produced constituents in the coating. Hence, it promotes the growth of metastable polymorphs of alumina, especially γ-Al_2O_3 phase [24]. The γ to α transformation is based on nucleation and growth and requires high temperatures; however, doping facilitates this transformation by influencing grain boundary diffusion and grain boundary mobility [43]. Transformation of γ-Al_2O_3 to α-Al_2O_3 occurs by changing the O^{2-} ion arrays from a cubic face-centered packing to a stable hexagonal packing and also realignment of Al^{3+} in octahedral holes by short-range diffusion [43,54]. Regarding the limited solubility of TiO_2 into Al_2O_3, segregation of TiO_2 cations at Al_2O_3 grain boundaries is expected [55]. In Al_2O_3 as a polar bonding crystal, diffusivity is controlled mostly by ionic bonding strength, which is changed by the segregation of the dopant cations. Dopant cations change the ionic strength by influencing on electron density map and vacancy [56]. Generally, increasing the ionicity between Al^{3+} and O^{2-} makes the increment of ionic bond. Comparing the energy level of atomic orbitals of Ti^{4+} with Al^{3+} and O^{2-} (energy level of 3d and 4s of Ti^{4+} is more than that of O 2p and less than that of Al 3p) shows the limited covalent interaction between Al^{3+} and Ti^{4+}. Thus, Ti^{4+} ions do not significantly affect the electron density distribution between Al^{3+} and O^{2-}. However, Ti^{4+} increases Al^{3+} vacancy, which reduces the ionicity in Al_2O_3 [56]. Then, ionic bond between Al^{3+} and O^{2-} weakens and grain boundary diffusion and grain boundary mobility, accommodated by grain boundary diffusion, will increase. Therefore, increasing the PTO concentration in the electrolyte bath raises the α-Al_2O_3 phase content in the coatings. The promotion of α-Al_2O_3 as a hard phase in the coating is an important result for tribological property of the coating where hardness has a significant effect on the wear resistance. Lack of α-Al_2O_3 in the coating prepared in Ref. [10], from solution containing solid TiO_2 nanoparticle, is attributed to the lower level of TiO_2 incorporated in the coating.

EIS results (Table 4) confirm that inner layer resistance is significantly higher than that of the outer layer and almost determines the overall corrosion resistance of P3 and P5 coatings. This is in agreement with the cross-section images of the coatings (Fig. 4), which confirm the compactness of the inner layers for these coatings. In contrast, it is observed that P0 and P1 specimens are lack of protective inner layers against penetration of the corrosive solution toward the substrate. As reported in Ref. [17], adding 3 g/L solid TiO_2 nanoparticles in the bath has an advantage to decrease the porosity of the coating produced by DC waveform, which improves the corrosion resistance. However, applying unipolar waveform in the same bath resulted in the larger micro-pores on the coating surface, which deteriorated the corrosion properties [10]. By comparison, it is found that a higher incorporation of TiO_2 is caused by DC waveform, which could improve the alumina sintering process. This decreases the cell voltage due to the increase of coating conductivity which prevents the destructive sparks.

As comprehended from Table 4, for P3 and P5 specimens, the CPE_{in} is higher than that of the outer layer. The capacitance of the coating layer is expressed as [57]

$$C = \frac{\varepsilon_0 \cdot \varepsilon \cdot S}{d} \tag{6}$$

where ε_0 and ε are the relative dielectric permittivities of the free space and the coating layer, respectively. S and d are the surface area and the thickness of the coating layer, respectively. The dielectric constant depends on density and phase constituents presented in the layer [18,58]. In general, higher density and lower porosity of the coating layer must result in a lower ε. On the other hand, the ε value of the coating layer is increased by adding TiO_2 due to the improved dielectric properties of Al_2O_3 by TiO_2 [59]. ZHANG et al [58] reported that the TiO_2 in Al_2O_3 is more effective on ε than the composite density. Thus, the higher CPE_{in} value than CPE_{out} obtained in EIS study (Table 4) confirms that the TiO_2 is dominantly located in the inner layer of the coatings, in agreement with the elemental maps of P3 and P5 specimens.

According to the electrochemical behavior of the coatings, 3 or 5 g/L PTO is required in the bath to reach the appropriate PEO coatings. Since the electrolyte containing 5 g/L PTO is not stable, and

some gray sediments appear at the bottom of the container through the coating process, the optimum PTO amount is considered to be 3 g/L.

5 Conclusions

(1) The incorporation of colloidal TiO_2 nanoparticles into the coating occurs through all types of micro-discharging. B-type micro-discharge results in the distribution of TiO_2 nanoparticles throughout the coating, while A-type and C-type micro-discharges dominantly distribute TiO_2 on top coating surface, and D-type ones facilitate the entrance of TiO_2 inside the inner layer.

(2) Continuous and thicker inner layers along with more coating compactness are resulted from higher PTO concentrations.

(3) The lower incorporation of TiO_2 into the coating increases the surface micro-pores, while its higher incorporation decreases the surface micro-pores.

(4) The incorporated TiO_2 nanoparticles encourage the α-Al_2O_3 phase formation.

(5) The TiO_2 in the PEO coating extends the passive region and raises the breakdown potential; this improves the localized corrosion resistance. In this way, the general corrosion resistance of the specimens is significantly improved. The reason is attributed to the formation of more compact and thicker inner layer.

References

[1] ZHANG Fan, ÖRNEK C, NILSSON J O, PAN Jin-shan. Anodisation of aluminium alloy AA7075 − Influence of intermetallic particles on anodic oxide growth [J]. Corrosion Science, 2020, 164: 108319.

[2] CHENG Ying-liang, XUE Zhi-gang, WANG Qun, WU Xiang-quan, MATYKINA E. New findings on properties of plasma electrolytic oxidation coatings from study of an Al−Cu−Li alloy [J]. Electrochimica Acta, 2013, 107: 358−378.

[3] YEROKHIN A L, VOEVODIN A, LYUBIMOV V V, ZABINSKI J, DONLEY M. Plasma electrolytic fabrication of oxide ceramic surface layers for tribotechnical purposes on aluminum alloys [J]. Surface and Coatings Technology, 1998, 110: 140−146.

[4] ARUNNELLAIAPPAN T, BABU N K, KRISHNA L R. RAMESHBABU N. Influence of frequency and duty cycle on microstructure of plasma electrolytic oxidized AA7075

and the correlation to its corrosion behavior [J]. Surface and Coatings Technology, 2015, 280: 136−147.

[5] BABAEI M, DEHGHANIAN C, VANAKI M. Effect of additive on electrochemical corrosion properties of plasma electrolytic oxidation coatings formed on CP Ti under different processing frequency [J]. Applied Surface Science, 2015, 357: 712−720.

[6] XIANG Nan, SONG Ren-gue, ZHUANG Jun-jie, SONG Rue-xi, LU Xiao-ya, SU Xu-ping. Effects of current density on microstructure and properties of plasma electrolytic oxidation ceramic coatings formed on 6063 aluminum alloy [J]. Transactions of Nonferrous Metals Society of China, 2016, 26: 806−813.

[7] AN Ling-yun, MA Ying, YAN Xiao-xu, WANG Sheng, WANG Zhan-ying. Effects of electrical parameters and their interactions on plasma electrolytic oxidation coatings on aluminum substrates [J]. Transactions of Nonferrous Metals Society of China, 2020, 30: 883−895.

[8] YEROKHIN A L, SHATROV A, SAMSONOV V, SHASHKOVE P, PILKINGTON A, MATTEWS L A. Oxide ceramic coatings on aluminium alloys produced by a pulsed bipolar plasma electrolytic oxidation process [J]. Surface and Coatings Technology, 2005, 199: 150−157.

[9] HUSSEIN R, NORTHWOOD D, SU Jun, NIE X W. A study of the interactive effects of hybrid current modes on the tribological properties of a PEO (plasma electrolytic oxidation) coated AM60B Mg-alloy [J]. Surface and Coatings Technology, 2013, 215: 421−430.

[10] HAKIMIZAD A, RAEISSI K, GOLOZAR M A, LU Xiao-peng, BLAWERT C, ZHELUDKEVICH M L. The effect of pulse waveforms on surface morphology, composition and corrosion behavior of Al_2O_3 and Al_2O_3/TiO_2 nano-composite PEO coatings on 7075 aluminum alloy [J]. Surface and Coatings Technology, 2017, 324: 208−221.

[11] TANG Ming-qi, LI Wei-ping, LIU Hui-cong, ZHU Li-qun. Influence of K_2TiF_6 in electrolyte on characteristics of the microarc oxidation coating on aluminum alloy [J]. Current Applied Physics, 2012, 12: 1259−1265.

[12] ALIRAMEZANI R, RAEISSI K, SANTAMARIA M, HAKIMIZAD A. Characterization and properties of PEO coatings on 7075 Al alloy grown in alkaline silicate electrolyte containing $KMnO_4$ additive [J]. Surface and Coatings Technology, 2017, 329: 1259−1265.

[13] LU Xiao-peng, MOHEDANO M, BLAWERT C, MATYKINA E, ARRABAL R, KAINER K U, ZHELUDKEVICH M L. Plasma electrolytic oxidation coatings with particle additions—A review [J]. Surface and Coatings Technology, 2016, 307: 1165−1182.

[14] LI Hong-xia, SONG Reng-guo, JI Zhen-guo. Effects of nano-additive TiO_2 on performance of micro-arc oxidation coatings formed on 6063 aluminum alloy [J]. Transactions of Nonferrous Metals Society of China, 2013, 23: 406−411.

[15] RAJ V, MUMJITHA M. Comparative study of formation

and corrosion performance of porous alumina and ceramic nanorods formed in different electrolytes by anodization [J]. Materials Science and Engineering B, 2014, 179: 25−35.

[16] SONG R G, WANG C, JIANG Y, LI H, LU G, WANG Z X. Microstructure and properties of Al_2O_3/TiO_2 nanostructured ceramic composite coatings prepared by plasma spraying [J]. Journal of Alloys and Compounds, 2012, 544: 13−18.

[17] BAHRAMIAN A, RAEISSI K, HAKIMIZAD A. An investigation of the characteristics of Al_2O_3/TiO_2 PEO nanocomposite coating [J]. Applied Surface Science, 2015, 351: 13−26.

[18] CAMPOS R V, BEZERRA C L, OLIVEIRA L N L, GOUVEIA D X. A study of the dielectric properties of $Al_2O_3−TiO_2$ composite in the microwave and RF regions [J]. Journal of Electronic Materials, 2015, 44: 4220−4226.

[19] IGNJATOVIĆ S, BLAWERT C, SERDECHNOVA M, KARPUSHENKOV S, DAMJANOVIĆ M, KARLOVA P, WIELAND D C F, STARYKEVICH M, STOJANOVIĆ S, DAMJANOVIĆ-VASILIĆ L J, ZHELUDKEVICH M L. Formation of multi-functional TiO_2 surfaces on AA2024 alloy using plasma electrolytic oxidation [J]. Applied Surface Science, 2021, 544: 148875.

[20] AKBARI E, DI FRANCO F, CERAOLO P, RAEISSI K, SANTAMARIA M, HAKIMIZAD A. Electrochemically-induced TiO_2 incorporation for enhancing corrosion and tribocorrosion resistance of PEO coating on 7075 Al alloy [J]. Corrosion Science, 2018, 143: 314−328.

[21] HAKIMIZAD A, RAEISSI K, SANTAMARIA M, ASGHARI M. Effects of pulse current mode on plasma electrolytic oxidation of 7075 Al in Na_2WO_4 containing solution: From unipolar to soft-sparking regime [J]. Electrochimica Acta, 2018, 284: 618−629.

[22] DEHNAVI V, LUAN Ben-li, LIU Xiang-yang, SHOESMITH D W, ROHANI S. Correlation between plasma electrolytic oxidation treatment stages and coating microstructure on aluminum under unipolar pulsed DC mode [J]. Surface and Coatings Technology, 2015, 269: 91−99.

[23] JIANG B L, WANG Y M. Plasma electrolytic oxidation treatment of aluminium and titanium alloys [M]//Surface Engineering of Light Alloys. Elsevier, 2010: 110−154.

[24] HAGHIGHAT-SHISHAVAN B, AZARI-KHOSROWSHAHI R, HAGHIGHAT-SHISHAVAN S, NAZARIAN-SAMANI M, PARVINI-AHMADI N. Improving wear and corrosion properties of alumina coating on AA7075 aluminum by plasma electrolytic oxidation: Effects of graphite absorption [J]. Applied Surface Science, 2019, 481:108−119.

[25] XIANG N, SONG R G, WANG C, MAO Q Z, GE Y J, DING J H. Formation of corrosion resistant plasma electrolytic oxidation coatings on aluminium alloy with addition of sodium tungstate species [J]. Corrosion Engineering, Science and Technology, 2016, 51: 146−154.

[26] LAVEISSIÈRE M, CERDA H, ROCHE J, CASSAYRE L, ARURAULT L. In-depth study of the influence of

electrolyte composition on coatings prepared by plasma electrolytic oxidation of TA6V alloy [J]. Surface and Coatings Technology, 2018, 361: 50−62.

[27] KOIRALA R, BUECHEL R, PRATSINIS S E, BAIKER A. Silica is preferred over various single and mixed oxides as support for CO_2-assisted cobalt-catalyzed oxidative dehydrogenation of ethane [J]. Applied Catalysis A: General, 2016, 527: 96−108.

[28] SANTAMARIA M, CONIGLIARO G, FRANCO F D, QUARTO F D. Photoelectrochemical evidence of Cu_2O/TiO_2 nanotubes hetero-junctions formation and their physicochemical characterization [J]. Electrochimica Acta, 2014, 144: 315−323.

[29] LEE H S, SINGH J K, ISMAIL M A. An effective and novel pore sealing agent to enhance the corrosion resistance performance of Al coating in artificial ocean water [J]. Scientific Reports, 2017, 7: 41935.

[30] USMAN B J, SCENINI F, CURIONI M. Corrosion testing of anodized aerospace alloys: Comparison between immersion and salt spray testing using electrochemical impedance spectroscopy [J]. Journal of the Electrochemical Society, 2020, 167: 041505.

[31] TAN Jian-hong, GUO Lei, YANG Hong, ZHANG Fan, EL BAKRI Y. Synergistic effect of potassium iodide and sodium dodecyl sulfonate on the corrosion inhibition of carbon steel in HCl medium: A combined experimental and theoretical investigation [J]. RSC Advances, 2020, 10: 15163−15170.

[32] PEZZATO L, BRUNELLI K, DABALÀ M. Corrosion properties of plasma electrolytic oxidation coated AA7075 treated using an electrolyte containing lanthanum-salts [J]. Surface and Interface Analysis, 2016, 48: 729−738.

[33] DEHNAVI V, SHOESMITH D W, LI B, YARI M, YANG X. Corrosion properties of plasma electrolytic oxidation coatings on an aluminium alloy−The effect of the PEO process stage [J]. Materials Chemistry and Physics, 2015, 161: 49−58.

[34] KARUPPUCHAMY S, SUZUKI N, ITO S, ENDO T. A novel one-step electrochemical method to obtain crystalline titanium dioxide films at low temperature [J]. Current Applied Physics, 2009, 9: 243−248.

[35] SALLEM F, VILLATTE L, GEFFROY P M, GOGLIO G, PAGNOUX C. Surface modification of titania nanoparticles by catechol derivative molecules: Preparation of concentrated suspension [J]. Colloids and Surfaces A: Physicochemical and Engineering Aspects, 2020, 602: 125167.

[36] TOORANI M, ALIOFKHAZRAEI M, ROUHAGHDAM A S. Microstructural, protective, inhibitory and semiconducting properties of PEO coatings containing CeO_2 nanoparticles formed on AZ31 Mg alloy [J]. Surface and Coatings Technology, 2018, 352: 561−580.

[37] TAKENAKA T, HABAZAKI H, KONNO H. Formation of black anodic films on aluminum in acid electrolytes containing titanium complex anion [J]. Surface and Coatings

Technology, 2003, 169−170: 155−159.

[38] LOPEZ-GARRITY O, FRANKEL G S. Corrosion inhibition of AA2024-T3 by sodium silicate [J]. Electrochimica Acta, 2014, 130: 9−21.

[39] HUSSEIN R, NIE X W, NORTHWOOD D. An investigation of ceramic coating growth mechanisms in plasma electrolytic oxidation (PEO) processing [J]. Electrochimica Acta, 2013, 112: 111−119.

[40] HUSSEIN R, NIE X W, NORTHWOOD D, YEROKHIN A, MATTHEWS A. Spectroscopic study of electrolytic plasma and discharging behaviour during the plasma electrolytic oxidation (PEO) process [J]. Journal of Physics D: Applied Physics, 2010, 43: 105203.

[41] BAGLEY R D, CUTLER I B, JOHNSON D L. Effect of TiO_2 on initial sintering of Al_2O_3 [J]. Journal of the American Ceramic Society, 1970, 53: 136−141.

[42] WANG Chih-Jen, HUANG Chi-Yuen. Effect of TiO_2 addition on the sintering behavior, hardness and fracture toughness of an ultrafine alumina [J]. Materials Science and Engineering A, 2008, 492: 306−310.

[43] LARTIGUE-KORINEK S, LEGROS C, CARRY C, HERBST F. Titanium effect on phase transformation and sintering behavior of transition alumina [J]. Journal of the European Ceramic Society, 2006, 26: 2219−2230.

[44] MILAK P C, MINATTO F D, de NONI A Jr, MONTEDO O R K. Wear performance of alumina-based ceramics—A review of the influence of microstructure on erosive wear [J]. Ceramica, 2015, 61: 88−103.

[45] TANG Ming-qui, LI Wei-ping, LIU Hui-cong, ZHU Li-qun. Influence of K_2TiF_6 in electrolyte on characteristics of the microarc oxidation coating on aluminum alloy [J]. Current Applied Physics, 2012, 12: 1259−1265.

[46] ELAISH R, CURIONI M, GOWERS K, KASUGA A, HABAZAKI H, HASHIMOTO T, SKELDON P. Effects of fluoride ions in the growth of barrier-type films on aluminium [J]. Electrochimica Acta, 2017, 245: 854−862.

[47] ZHU Lu-jun, GUO Zhen-xi, ZHANG Yue-fei, LI Zheng-xian, SUI Man-ling. A mechanism for the growth of a plasma electrolytic oxide coating on Al [J]. Electrochimica Acta, 2016, 208: 296−303.

[48] CHENG Ying-liang, CAO Jin-hui, MAO Mo-ke, XIE Huan-jun, SKELDON P. Key factors determining the development of two morphologies of plasma electrolytic coatings on an Al−Cu−Li alloy in aluminate electrolytes [J]. Surface and Coatings Technology, 2016, 291: 239−249.

[49] SNIZHKO L O, YEROKHINA L, GUREVINA N L,

PATALAKHA V A, MATTHEWS A. Excessive oxygen evolution during plasma electrolytic oxidation of aluminium [J]. Thin Solid Films, 2007, 516: 460−464.

[50] YANG Kai, HUANG Hai-song, CHEN Jia-dui, CAO Biao. Discharge behavior and dielectric breakdown of oxide films during single pulse anodizing of aluminum micro-electrodes [J]. Materials (Basel), 2019, 12: 2286.

[51] SNIZHKO L O, YEROKHINA L, PILKINGTON A, GUREVINA N L, MISNYANKIN D O, LEYLAND A, MATTHEWS A. Anodic processes in plasma electrolytic oxidation of aluminum in alkaline solutions [J]. Electrochimica Acta, 2004, 49: 2085−2095.

[52] CHENG Ying-liang, MAO Mo-ke, CAO Jin-hui, PENG Zhao-mei. Plasma electrolytic oxidation of an Al−Cu−Li alloy in alkaline aluminate electrolytes: A competition between growth and dissolution for the initial ultra-thin films [J]. Electrochimica Acta, 2014, 138: 417−429.

[53] BARATI N, YEROKHIN A, GOLESTANIFARD F, RASTEGARI S, EFSTATHIOS E I. Alumina−zirconia coatings produced by plasma electrolytic oxidation on Al alloy for corrosion resistance improvement [J]. Journal of Alloys and Compounds, 2017, 724: 435−442.

[54] XUE L A, CHEN I W. Influence of additives on the $γ$- to $α$-transformation of alumina [J]. Journal of Materials Science Letters, 1992: 443−445.

[55] CHOI J L, HAN J H, KIM D Y. Effect of titania and lithia doping on the boundary migration of alumina under an electric field [J]. Journal of American Ceramic Society, 2003, 86: 347−350.

[56] YOSHIDA H, IKUHARA Y, SAKUMA T. Grain boundary electronic structure related to the high-temperature creep resistance in polycrystalline Al_2O_3 [J]. Acta Materialia, 2002, 50: 2955−2966.

[57] van SCHAFTINGHEN T, PEN C L, TERRYN H, HÖRZENBERGER F. Investigation of the barrier properties of silanes on cold rolled steel [J]. Electrochimica Acta, 2004, 49: 2997−3004.

[58] ZHANG Qi-long, YANG Hui, ZOU Jia-li, SUN Hui-ping. Sintering and dielectric properties of Al_2O_3 ceramics doped by TiO_2 and CuO [J]. Journal of Electroceramics, 2007, 18: 225−229.

[59] LIU Qing-rong, QIU Ming-bo, SHEN Li-de, JIAO Chen, YE Yun, XIE De-qiao, WANG Chang-jiang, XIAO Meng, ZHAO Jian-feng. Additive manufacturing of monolithic microwave dielectric ceramic filters via digital light processing [J]. Electronics, 2019, 8: 1067−1081.

TiO₂ 纳米颗粒对 7075 铝合金表面等离子体电解氧化涂层性能的影响

Mehri HASHEMZADEH[1], Keyvan RAEISSI[1], Fakhreddin ASHRAFIZADEH[1],
Amin HAKIMIZAD[2], Monica SANTAMARIA[3]

1. Department of Materials Engineering, Isfahan University of Technology, Isfahan 84156-83111, Iran;
2. Yekta Mobaddel Pars Co., Science and Technology Campus, Yazd University, Yazd 89158-18411, Iran;
3. Dipartimento di Ingegneria, Università di Palermo, Viale Delle Scienze, Ed. 6, 90128, Palermo, Italy

摘　要：采用等离子体电解氧化(PEO)技术，利用单极脉冲波形在含有胶体 TiO₂ 纳米颗粒的溶胶电解液中制备 Al₂O₃−TiO₂ 复合涂层。溶胶溶液是将 1、3 和 5 g/L 的草酸钛酸钾(PTO)溶解在硅酸盐溶液中制得。利用扫描电镜、能量色散光谱、X 射线衍射和拉曼光谱对涂层进行表征。采用极化和阻抗技术研究涂层的腐蚀行为。结果表明，TiO₂ 通过微放电方式进入涂层，并掺杂到氧化铝相中。TiO₂ 掺入量较高时，表面微孔减少；反之，掺入量较低时则微孔增多。TiO₂ 含量越高，涂层的外层越致密，内层越厚。电化学测试结果表明，与在不含 PTO 溶液中制备的涂层相比，在含 3 g/L PTO 溶液中制备的涂层腐蚀性能得到大幅提高。在不含 PTO 溶液中制备的涂层含有 γ-Al₂O₃，δ-Al₂O₃ 和非晶相，而 PTO 的存在促进 α-Al₂O₃ 的生成。

关键词：铝合金；Al₂O₃−TiO₂ 涂层；等离子体电解氧化；草酸钛酸钾；耐蚀性

(Edited by Bing YANG)